



Influence of cooling water temperature on ME20M magnesium alloy submerged friction stir welding: a numerical and experimental study

Wenming Liu¹ · Yinfei Yan¹ · Tao Sun¹ · Siyu Wu¹ · Yifu Shen¹

Received: 6 May 2019 / Accepted: 20 September 2019 / Published online: 18 November 2019
© Springer-Verlag London Ltd., part of Springer Nature 2019

Abstract

Submerged friction stir welding on magnesium (Mg) alloy is investigated with limits in the past. ME20M is an important lightweight Mg alloy with enhanced yield strength and heat resistance that merits further research. In this paper, submerged friction stir welding of ME20M Mg alloy was carried out in different temperatures of cooling water. Three-dimensional numerical was employed to analyze the thermal field under the same weld conditions, and the numerical predictions were compared with the experimental results. The macrostructure, microstructure, tensile properties, and hardness are tested. The results show that the numerical results and the experimental results exhibits the same trends. By increasing the cooling water temperature, the grain size of the weld nugget increased, the tensile strength of the joint decreased, and the microhardness of the weld joint decreased. The largest tensile strength was 170.5 MPa, which was ~ 71.04% of the base metal. The highest and the lowest hardness values of the weld joint were obtained at the cooling water temperature of 15 °C and 75 °C, respectively, in the weld nugget and heat-affected zones.

Keywords Submerged friction stir welding · ME20M magnesium alloy · Simulated · Microstructure · Mechanical properties

1 Introduction

Magnesium (Mg) alloys are increasingly important lightweight structure materials for application in many industries [1]. However, Mg alloys was still limited, applied by their poor formability, which can be enhanced by grain refining. During the research and development of Mg alloys, Al, Zn, or Mn were added in different ratios to improve their formability. Furthermore, improvements in the formability of Mg alloys have been demonstrated by the addition of rare earth (RE) elements, such as cerium (Ce) and lanthanum (La) [2–5]. Among all of the Mg-RE alloys, ME20M Mg alloy (also previously known as MB8), which contains manganese (Mn) and Ce, own its advantage in weldability and corrosion resistance and was extensively employed in aircraft envelope and panels [6].

Friction stir welding (FSW) was invented in 1991 as an effective method to produce high-quality grain refined joints [7]. Many researchers had studied Mg alloys through the methods of friction stir welding/processing (FSW/P), especially the RE-Mg alloys [8–13]. They found that microstructure characterization revealed significant grain refinement; ultimate strength was primarily attributed to macroscopic features. FSW/P of ME20M Mg alloy was carried out by many researchers; observed that the grain size was refined from about 16.5–6 μm, the tensile strength of the defect-free joint was ~ 76% of the base metal; the microhardness and elongations of the joint were also increased in some degree, respectively [14–16]. Since fine-grained microstructures generally improved the material's strength and plasticity, a certain cooling method (such as water cooling) which can achieve even finer grain sizes was adopted in FSW and named submerged friction stir welding (SFSW). AZ31 [17], AZ61 [18], and AZ91 [19] Mg alloys were welded by FSW/P in air and underwater and then investigated the microstructures and mechanical properties. Grains obtained by SFSW was finer than FSW in air; the mechanical properties were also improved by

✉ Yifu Shen
yfshen_nuaa@hotmail.com

¹ College of Material Science and Technology, Nanjing University of Aeronautics and Astronautics (NCAA), Jiangjun Road 29, Nanjing 210016, People's Republic of China

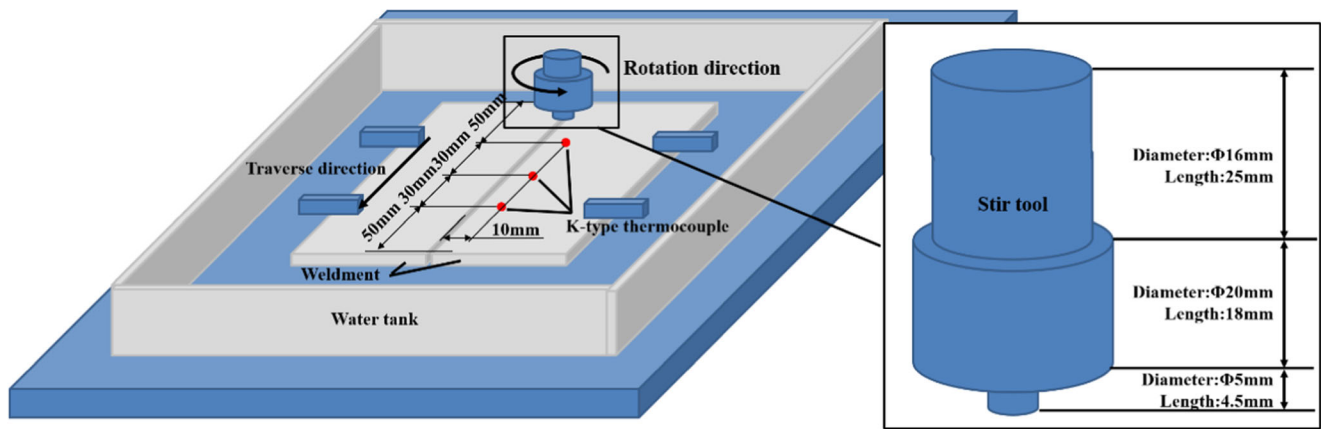


Fig. 1 Fixture diagram and the stir tool of submerged friction stir welding

water cooling. Furthermore, the cooling rate was known as an important influence factor during the cooling process of the melt metals. Though the FSW is a solid diffusion bonding, the cooling rate cannot be ignored and has attracted some interest. Based on the above consideration, different water cooling environment was discussed in hot water and cold water [20]. The results indicated that the joints welded in hot water were improved to own the best mechanical properties, but it had the biggest width of the minimum hardness accordingly with the heat-affected zone (HAZ) of the joints.

Due to the convenience and feasibility of the numerical simulations, numerical investigations were used in FSW/P; many researchers tended to simulate the complex details such as heat generation, metal fluent, and mass transfer for process set-up and welding history prediction [21, 22]. Friction stir welding of AZ31 Mg alloy was simulated in the thermos process and was compared with the experimental temperature [23]. Discrepancies between numerical and experimental temperature values were little, and the results were in good agreement. The microstructure evolution, temperature, and effective strain

distributions of AZ91Mg alloy FSW were analyzed by using the software Deform-3D [24, 25], and the simulation results could exactly reflect the experimental temperature and predict the effective strain distributions. The simulated microstructures were in good agreement with experimental microstructure. ANSYS was also used to simulate the FSW thermos history both in air and immersed conditions [26]; the thermal numerical temperature results in the weld nugget zone were within a 3.5% error, which improved the prediction of the temperature history.

ME20M Mg alloy is extensively applied in many industries because of its excellent properties, however, it has been minimally studied to date. In this study, ME20M was employed to carry out the submerged friction stir welding to research the effects of the water cooling environment on the welding joints. To further study the temperature history and have a better understanding of the influence of water cooling on the results, numerical simulation was proceeded and compared with the experimental results. Besides, microstructure and mechanical properties of the weld joints were discussed in detail.

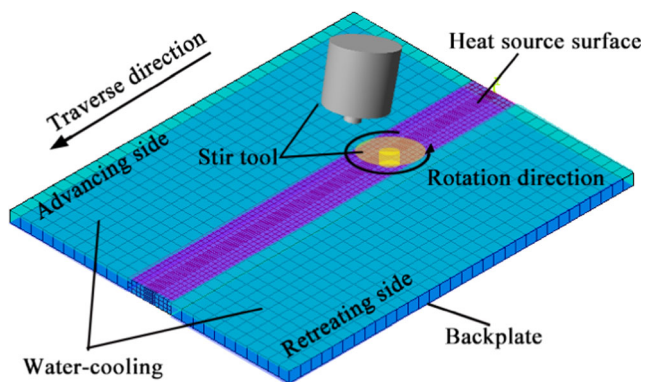


Fig. 2 Mesh graph of the simulate model in submerged friction stir welding

Table 1 Material properties of the ME20M Mg alloy

Density (ρ)	1.78 g cm ⁻³	
Specific heat (c)	250 J/(kg K)	
Poisson's ratio	0.34	
Heat conductivity coefficient (λ)	32 W/(m K)	
Elasticity modulus (E)	41,000 MPa	
Linear expansion coefficient (α)	20~100 °C	$23.61 \times 10^{-6}/^{\circ}\text{C}$
	100~200 °C	$26.1 \times 10^{-6}/^{\circ}\text{C}$
	200~300 °C	$32.0 \times 10^{-6}/^{\circ}\text{C}$
Tensile strength (vertical) (σ_b)	240 MPa	

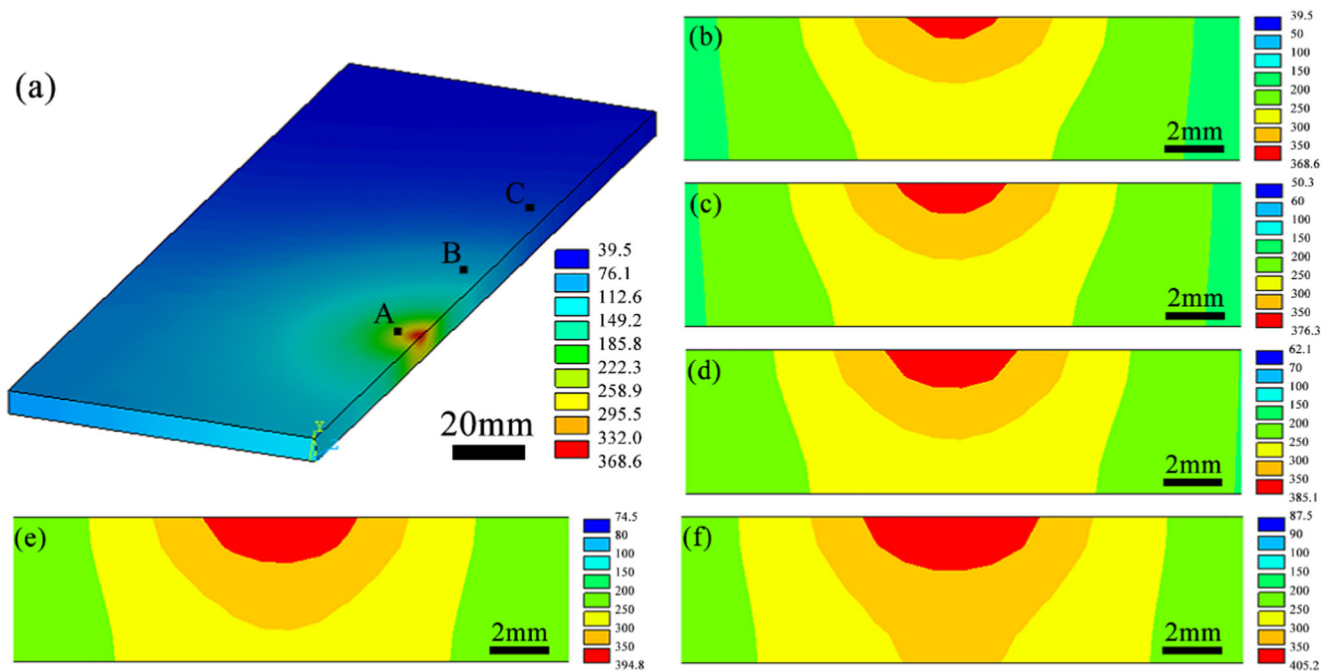


Fig. 3 Simulated temperature field of the different cooling water temperatures. Whole temperature distribution of 15 °C (a)°C;. Partial temperature distribution of (b) 15 °C (b);, of (c) 30 °C (c);, of (d) 45 °C (d)°C;. of (e) 60 °C (e);,°C; and of (f) 75 °C (f)

2 Material and experiments

The material under investigation was ME20M Mg alloy plates based on the Mg matrix with the addition of 0.15~0.35 wt% Ce, 1.3~3.2 wt% Mn, ≤ 0.20 wt% Aluminum (Al), ≤ 0.30 wt% Zinc (Zn), ≤ 0.10 wt% Silicon (Si), ≤ 0.05 wt% Iron (Fe), and ≤ 0.05 wt% Copper (Cu). The dimensions of the plates are 5-mm thick, 160-mm long, and 65-mm wide, respectively. The stir tool was made of H13 steel, and be quenching and tempering treated to ameliorate the friction and stir ability. The welding of the ME20M Mg alloys was undertaken on a CNC milling center in a butt configuration and placed in a container that held the samples submerged during the welding process as shown in Fig. 1. Flowing water was used to keep the cooling water temperature. After series of experiments, 1300 rpm rotation speed, 40 mm/min traverse speed, and 0.3 mm plunge depth were chosen to be the process parameters, and the temperature of the cooling water changed from 15 to 75 °C spacing of 15 °C. K-type thermocouples were fixed at the top surface and 10 mm from the weld line on the retreating side.

For the metallographic specimen preparation, the samples were cut perpendicular to the welding direction by wire electrode cutting and etched with an acetic-picric solution composed of 10 ml acetic acid, 4.2 g picric acid, 10 ml water, and 70 ml ethanol (95%). The samples were then characterized by a QMW550 digital optical

microscope and QVANTA 650 scanning electron microscope (SEM).

The microhardness of the joints tested on an HXS-1000A microhardness testing machine by applying a load of 100 g and a dwell time of 15 s along the centerline of the thickness direction with a 0.5 mm spacing between each point. Tensile tests in accordance with the ASTM E8/E8M standard were carried out using a CMT 5105 SANS microcomputer-controlled electronic universal tensile testing machine (Shenzhen SANS Metering Technology). The tensile strength results were recorded, and the average value of the two specimens was calculated. The fracture surfaces of the tensile samples were identified by SEM.

3 Numerical modeling

3.1 Model description

The 3D simulation software ANSYS was used to simulate the thermos history of ME20M Mg alloy SFSW in different water cooling conditions. Solid 70, an eight-node hexahedral element with only one temperature freedom degree for each node, was chosen to be the finite element. The mesh graph as illustrated in Fig. 2 has the finest grids in the stir zone, the finer grids in the shoulder-affected zone, and the largest grids in the

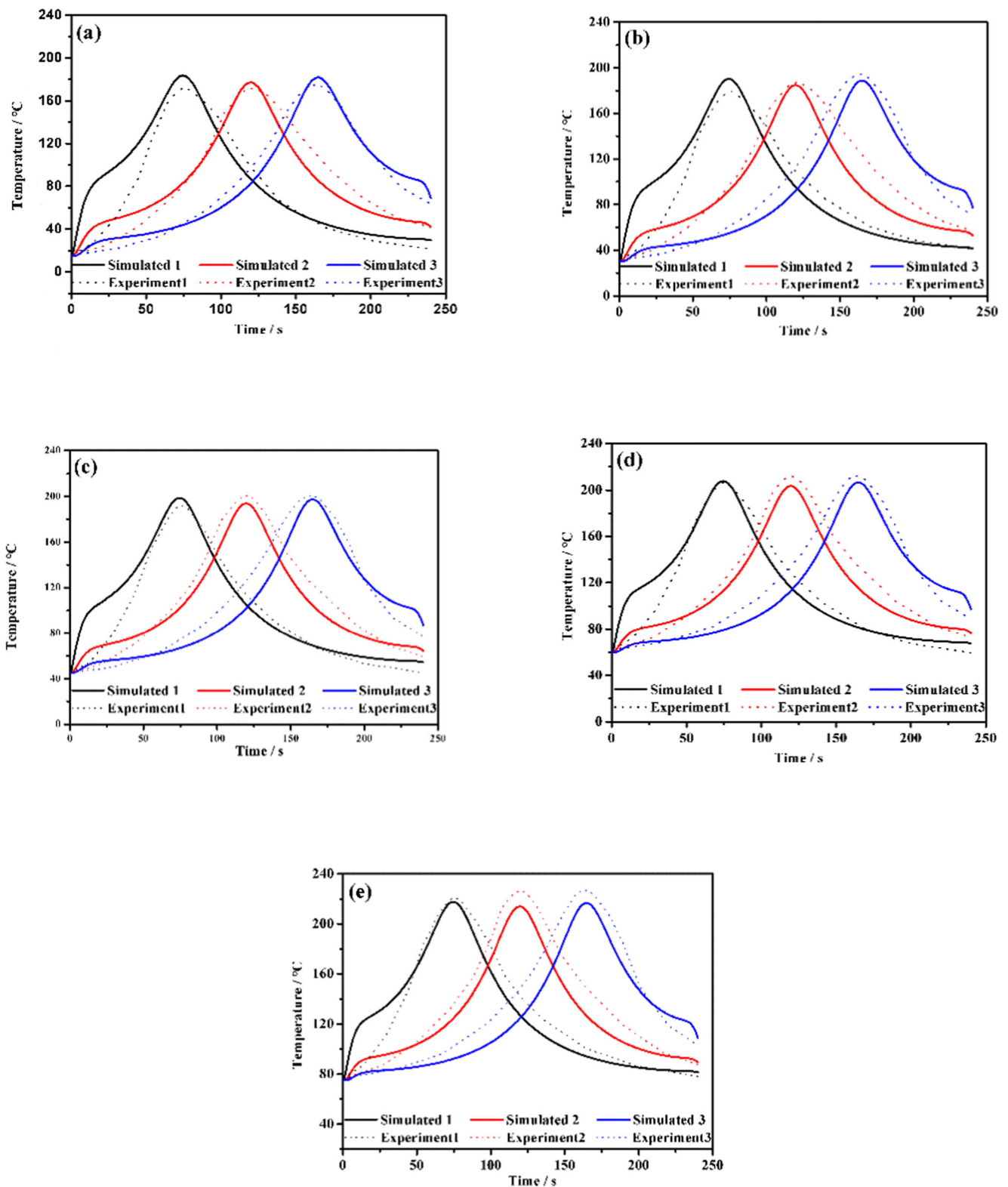


Fig. 4 Temperature-time curves of the different cooling water temperatures. **a** 15 °C. **b** 30 °C. **c** 45 °C. **d** 60 °C. **e** 75 °C

other area to balance the calculation accuracy and calculation time. The physical properties of ME20M Mg alloy were shown in Table 1. Besides, it was assumed that

1. The workpiece is modeled as an isotropic and homogeneous material.
2. The friction factor between the workpiece and the tool is constant.

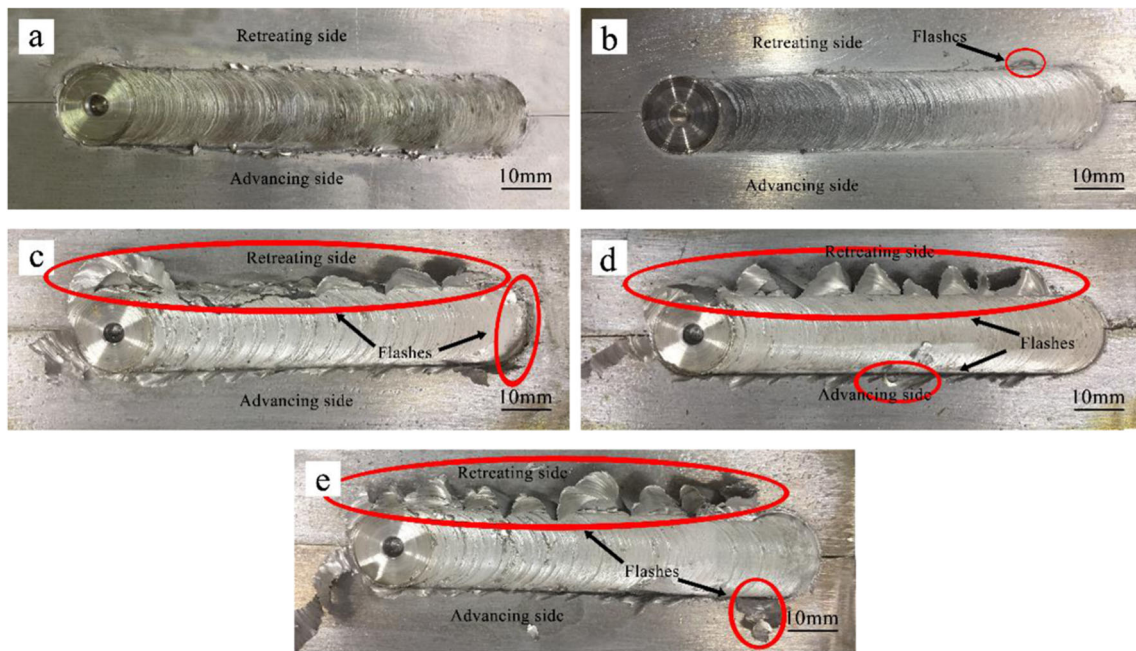


Fig. 5 Surface of the friction stir welded joint in different cooling water temperature. **a** 15 °C. **b** 30 °C. **c** 45 °C. **d** 60 °C. **e** 75 °C

3. The thermal characteristics of the workpiece and tool are constant.

Besides, the stir tool model was the same dimensions of the experiments. During the experiments, the tool also heated by the friction heat of the tool and the workpiece, which may experience heat transfer during the experiment [27, 28]. Compared with the other heat transfer, the heat transfer between the tool and the workpiece could be ignored. Thus, to save the calculation accuracy and calculation time, the stir tool geometry was simplified.

3.2 Boundary conditions and material properties

Radiation, convection, and heat conduction are the basic method of heat transfer. For FSW, the main heat transfer is heat conduction. Therefore, the basic equation of heat transfer in the temperature field is mainly derived by the differential equation of heat conduction. FSW heat transfer is a typical three-dimensional transient heat transfer process due to the thermal properties of its material as a function of temperature.

For the nonlinear transient heat transfer process, the basic equation is as follows:

$$\rho c \frac{\partial T}{\partial t} - \frac{\partial}{\partial x} \left(\lambda \frac{\partial T}{\partial x} \right) - \frac{\partial}{\partial y} \left(\lambda \frac{\partial T}{\partial y} \right) - \frac{\partial}{\partial z} \left(\lambda \frac{\partial T}{\partial z} \right) - \rho Q = 0 \quad (1)$$

where ρ is the density (kg/m^3), c is the specific heat capacity (J/kg K), t is the time of the welding, λ is the heat conduction coefficient (W/m K), and Q is the heat source density (W/kg).

As we know, the heat source of the FSW concludes two parts, i.e., friction heat and material plastic deformation heat. According to the literature, friction heat can be divided into friction heat generated between the shoulder and the weldment, the pin side surface and the weldment, and the pin bottom surface and the weldment [29, 30].

The heat generated by the two parts can be written as:

$$Q = \delta Q_f + (1-\delta)Q_p \quad (2)$$

where δ is the contact state variable, Q_f is the heat generated by friction, and Q_p is the heat generated by plastic deformation.

When $\delta = 1/0$, heat is generated only by friction or plastic deformation, and the heat is generally generated by both of them, but friction heat is the main one. Different mechanisms of heat generation are behind different contact condition, which are described as sliding, sticking, or partial sliding/sticking [31, 32]. During the SFSW, different parts of the stir tool and workpiece are behind different mechanisms. In this study, δ was assumed to be a different value because of the different ratios of heat generated by friction and plastic deformation. The heat flux (W/m^2) of all the heat generated by the friction heat and material plastic deformation can be expressed as:

$$q = q_1 + q_2 + q_3 \quad (3)$$

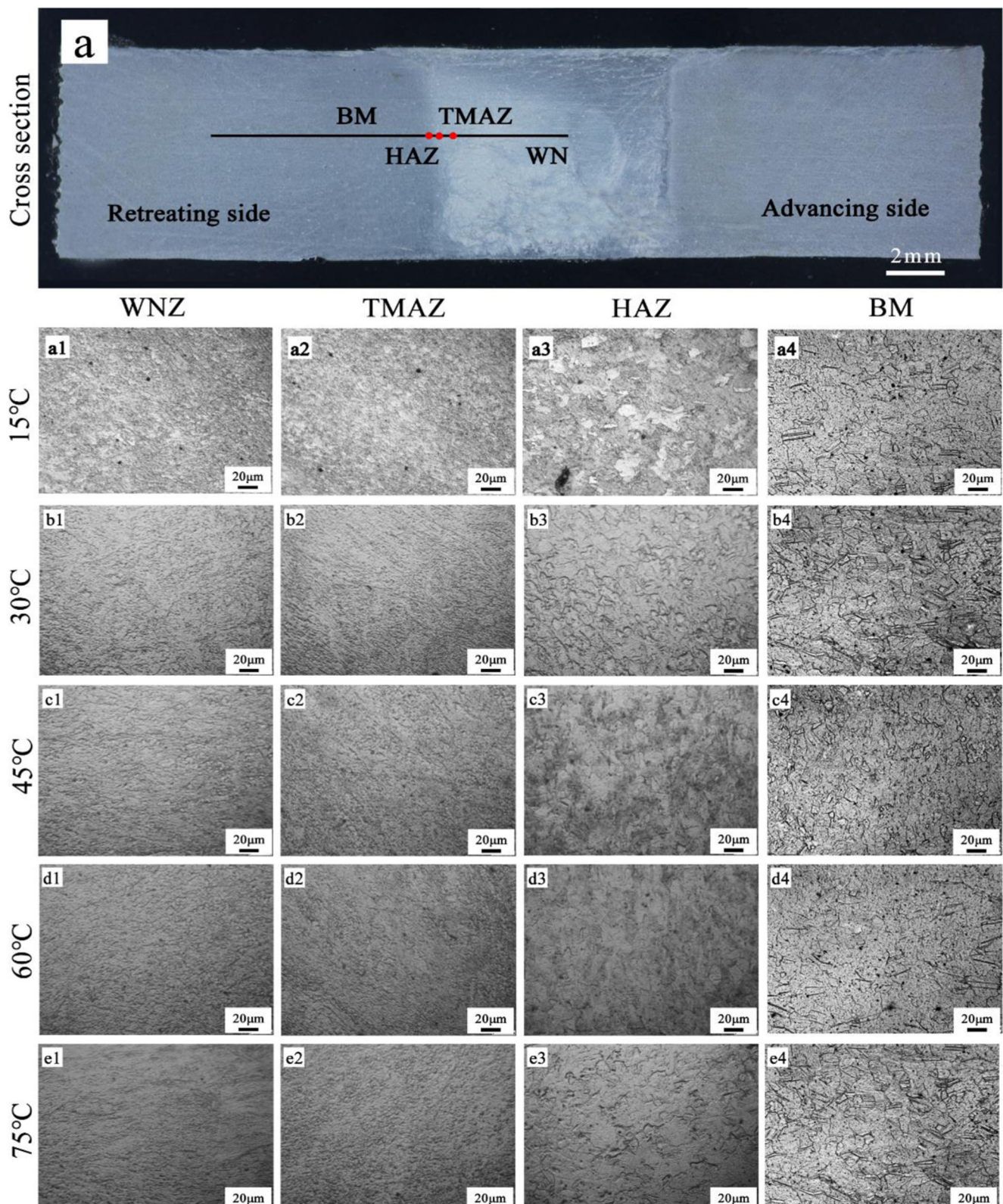


Fig. 6 Typical cross-section and the microstructures in different cooling water temperatures

where q_1 is the heat generated by shoulder and weldment, q_2 is the heat generated by pin side surface and

weldment, and q_3 is the heat generated by pin bottom and weldment.

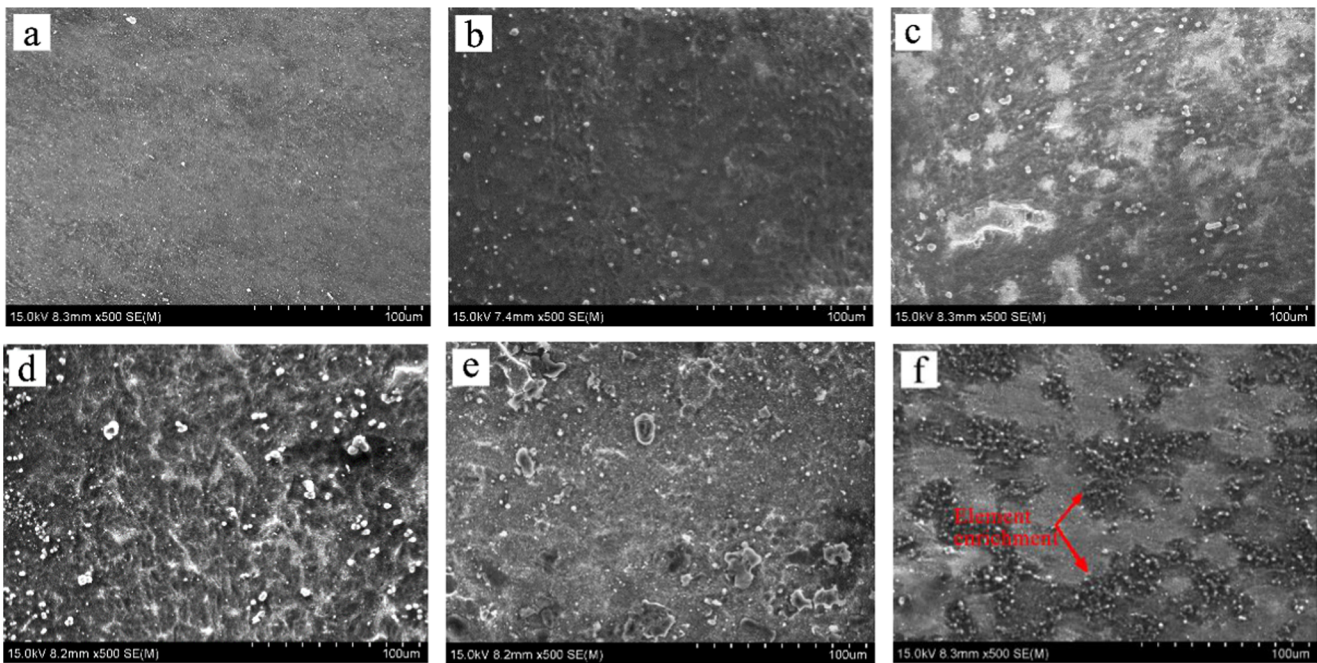


Fig. 7 SEM results of the HAZ and BM in different cooling water temperatures. a 15 °C. b 30 °C. c 45 °C. d 60 °C. e 75 °C. f BM

The maximum shear stress for yielding was assumed to be:

$$\tau_b = \frac{\sigma_s}{\sqrt{3}} \tag{4}$$

where σ_s is the yield stress of ME20M Mg alloy.

In this case, the heat generated by the shoulder is written as:

$$\begin{aligned} Q_1 &= \delta_1 \omega \int_{R_2}^{R_1} \tau_b \cdot 2\pi r^2 dr + (1-\delta_1) \omega \int_{R_2}^{R_1} \mu P \cdot 2\pi r^2 dr \\ &= [\delta_1 \tau_b + (1-\delta_1) \mu P] \cdot \frac{2}{3} \pi \omega (R_1^3 - R_2^3) \end{aligned} \tag{5}$$

The heat flux (W/m²) at the shoulder and weldment is

$$\begin{aligned} q_1 &= \frac{Q_1}{\pi(R_1^2 - R_2^2)} \\ &= \frac{[\delta_1 \tau_b + (1-\delta_1) \mu P] \cdot 2\omega(R_1^2 + R_2^2 + R_1 R_2)}{3(R_1 + R_2)} \end{aligned} \tag{6}$$

where δ_1 is the contact state variable, assumed to be 0.35; μ is the coefficient of friction, assumed to be 0.4; P is the plunge pressure (Pa); and ω is the rotation speed (r/s).

The heat generated by the pin side surface and weldment is written as:

$$\begin{aligned} Q_2 &= \delta_2 \omega \int_0^H \tau_b \cdot 2\pi R_2^2 dh + (1-\delta_2) \omega \int_0^H \mu P_1 \cdot 2\pi R_2^2 dh \\ &= [\delta_2 \tau_b + (1-\delta_2) \mu P_1] 2\pi \omega R_2^2 H \end{aligned} \tag{7}$$

The heat flux (W/m²) at the pin side surface and weldment is

$$q_2 = \frac{Q_2}{2\pi R_2 H} = [\delta_2 \tau_b + (1-\delta_2) \mu P_1] \omega R_2 \tag{8}$$

where δ_2 is the contact state variable, assumed to be 0.5; H is the height of the tool pin; and P_1 is the measured approach of the plunge pressure P .

The heat generated by the pin bottom and weldment is written as:

$$\begin{aligned} Q_3 &= \delta_3 \omega \int_0^{R_2} \tau_b \cdot 2\pi r^2 dr + (1-\delta_3) \omega \int_0^{R_2} \mu P \cdot 2\pi r^2 dr \\ &= [\delta_3 \tau_b + (1-\delta_3) \mu P] \cdot \frac{2}{3} \pi \omega R_2^3 \end{aligned} \tag{9}$$

The heat flux (W/m²) at the pin bottom and weldment is

$$q_3 = \frac{Q_3}{\pi R_2^2} = \frac{2\omega R_2}{3} [\delta_3 \tau_b + (1-\delta_3) \mu P] \tag{10}$$

where δ_3 is the contact state variable, assumed to be 0.35.

The boundary conditions describe the characteristics of the heat transfer process at the boundary of the objects [33–36]. The heat transfer methods include heat conduction, heat radiation, and heat convection. Heat conduction is a heat transfer mode that occurs primarily in solids, and heat convection is primarily a unique way of heat transfer in liquids and gases. It was assumed that heat radiation is ignored during the FSW, so only the heat conduction and heat convection are considered. Calculated total heat flux using Eqs. 2–10 is applied on the surfaces of the elements, where the Gauss heat source was employed as shown in

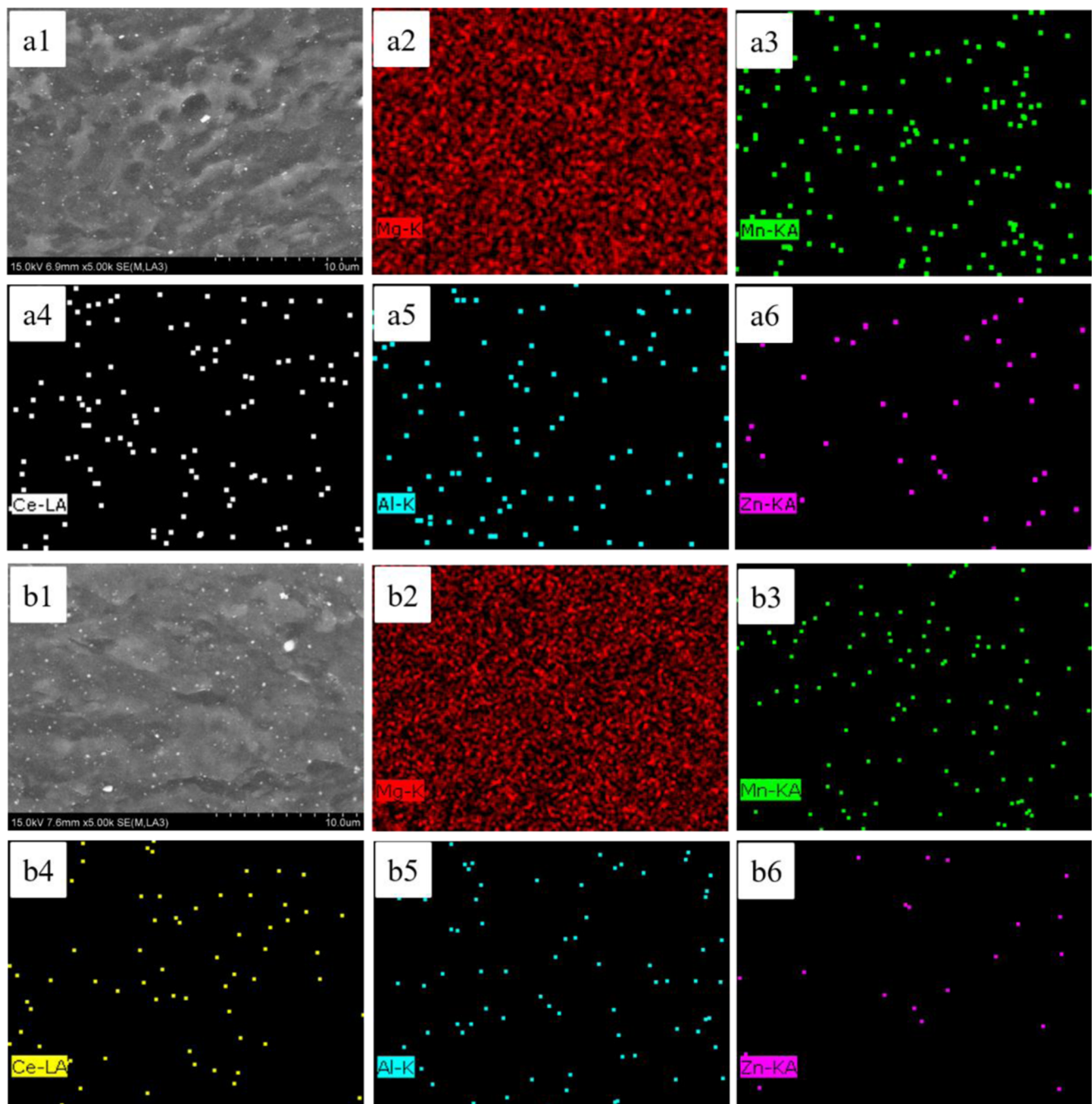


Fig. 8 SEM and EDS results of the weld nugget in different water temperature. a 15 °C. b 75 °C

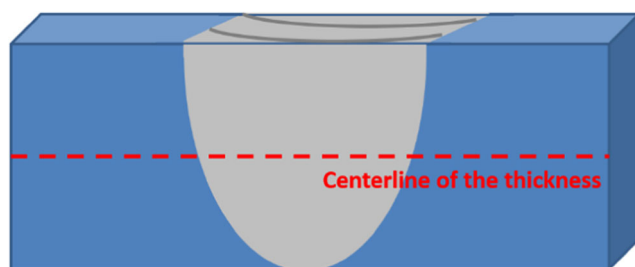


Fig. 9 Schematic diagram of the hardness points

Fig. 2. Before the FSW welding, the workpiece temperature distribution was uniform and equal to the ambient temperature, taking the cooling water temperature to be the ambient temperature. The workpiece contacts with the water and back plate meeting the boundary conditions of thermal convection. The convective heat transfer coefficient of the back plate is set to $150 \text{ W}/(\text{m}^2 \text{ K})$. For the top surface near the welding tool, the contact water is in the boiling state under the effect of elevated temperature, leading to intense heat transfer between the workpiece and

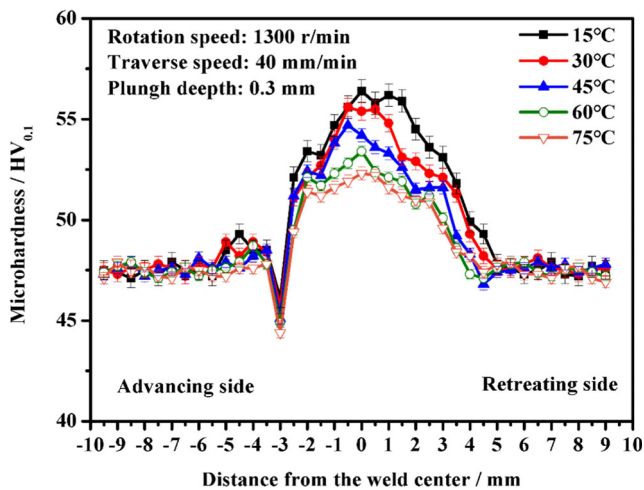


Fig. 10 Microhardness of the weld joint along the center line of thickness direction

boiling water [37]. Because of the different conditions of water vaporization, the convective heat transfer coefficient of the cooling water is set to different parameters, ranging from 250 to 500 W/(m² K).

4 Result and discussion

4.1 Heat generation and temperature distribution

The temperature histories were simulated according to the experiments under the same environment during the SFSW in the different cooling water environment. The experimental results were also recorded to compare with the simulated results. The simulated temperature fields and the position of measured points are shown in Fig. 3. From Fig. 3a, the temperature gradient is higher in front of the tool than behind. Figure 3b–f illustrates the partial temperature field of the weld joint. The results showed that the temperature decreased along the thickness direction from the top to the bottom of the weldment, which was because the heat was generated mainly by the friction of the shoulder and the weldment, and the convection coefficient between the weldment and the cooling water. With the increase of the cooling water temperature, the peak temperature of the weld nugget increased from 368.6 to 405.2 °C, lower than the material solidus temperature of 649 °C, at which temperature, there were no melt

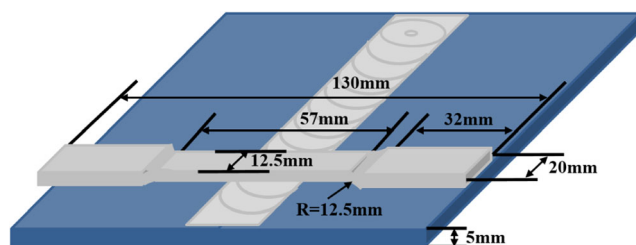


Fig. 11 Dimension of the tensile samples

materials. The temperature-time curve comparison between the numerical results of the HAZ and experimental results is illustrated in Fig. 4. Figure 4a–e shows the temperature-time curves in different water cooling temperature. The solid lines expressed the numerical results; simulated 1, simulated 2, and simulated 3 were the simulated temperature-time curves of points A, B, and C of Fig. 3a, respectively. Experiment 1, experiment 2, and experiment 3 in dotted lines exhibited the same points of the experimental results. From the curves, the temperature of the numerical results and the experimental results showed the same trends and were closed; the calculated difference of the numerical values and the experimental values were almost less than 5%, but there were some large difference at the decline range of the curves, which may be caused by unstable cooling water temperature. In general, the difference of the curves was approached, which indicated that the model can nearly accurately predict the temperature history in the SFSW process. The temperature history of different K thermocouple points experienced the process closed to each other. As the cooling water temperature rises, the peak temperature of the temperature histories increases, which indicated that the temperature of the cooling water affected the heat generation of the welding process.

4.2 Macro and microstructure

During the SFSW process, the rotation of the stir tool leads to severe plastic deformation, and the plastic materials flow from the advancing side (AS) to the retreating side (RS). Figure 5 illustrates the weld surface of the different conditions. Because of the axial force of the tool, flash defects formed when the materials were pushed out. The quantity of the flashes increases as the cooling water temperature increases. It was totally attributed to the increased weld temperature that result to more materials being plasticized and ejected to the outside [38]. The flashes at the RS were more than that of the AS, which was because the AS had a higher temperature than the RS; the metals flowed fluently from the AS to the RS and then ejected to the outside. The typical cross-section and the microstructures in different cooling water temperatures are shown in Fig. 6. There are four regions in an FSW joint, i.e., base metal (BM), HAZ, thermo-mechanically affected zone (TMAZ), and weld nugget (WN). Figure 6a shows the cross-section of the FSW joint; the four regions were identified. Figure 6 a1, b1, c1, d1, and e1 is the WN of the joints in different temperatures of the cooling water, which experienced a strong stirring, high-temperature thermal cycle, and dynamic recrystallization. In the reason of the small difference in the peak temperature, the microstructure exhibited a tiny difference. The grain sizes were much finer than the TMAZ as shown in Fig. 6 a2, b2, c2, d2, and e2, which underwent the bending deformation and reversion reactions. With the improvement of the weld temperature, the grains grow up, but the effects were limited. The region that only affected by the

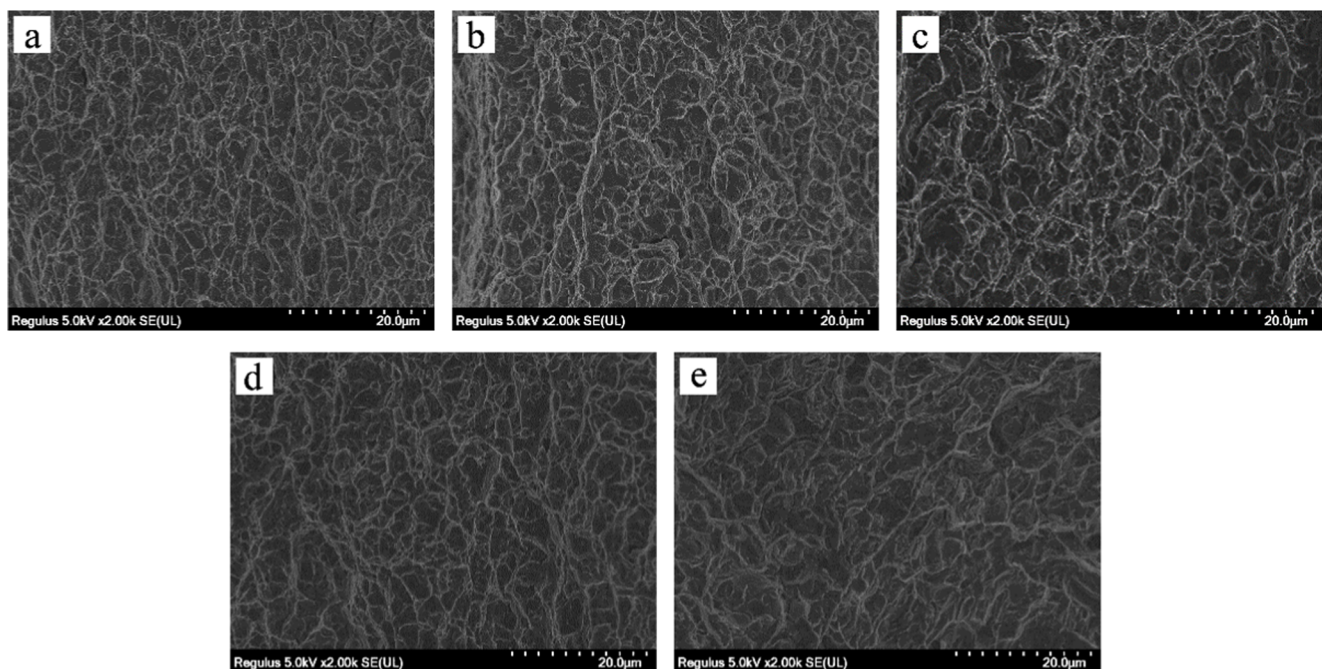
Table 2 Tensile results of submerged friction stir welding

Cooling water temperature	Average tensile strength (MPa)	Performance	Fracture position
15 °C	166.0, 175.0 (170.5)	71.04%	HAZ of AS
30 °C	172.8, 162.7 (167.8)	69.90%	HAZ of AS
45 °C	168.4, 164.4 (166.4)	69.33%	HAZ of AS
60 °C	163.7, 161.5 (162.6)	67.75%	HAZ of AS
75 °C	161.8, 160.1 (161.0)	67.06%	HAZ of AS

thermal cycle was HAZ, which may cause the strength decreased, is shown in Fig. 6 a3, b3, c3, d3, and e3. Due to the effects of the water cooling, the HAZ was not obvious to be found. Investigations have revealed that the HAZ gets a narrow precipitate free zone, along the grain boundary, which attributes to a lower level of precipitate coarsening under water cooling and exert negative effects on the mechanical properties of the materials [39]. With the increase in the temperature of the cooling water, the HAZ became more clearly to distinguish from the BM; the grain sizes increased by the increase of the cooling water temperature. The BM revealed recrystallized $\alpha + \beta$ (Mn) microstructure, fine grains distributed at coarse grain boundaries, and precipitated phase were found at the boundary of the grains, are shown in Fig. 6 a4, b4, c4, d4, and e4.

As we know, the distribution of elements decided the properties of the materials. Mn, Ce, Zn, and Al act as different properties improving roles, such as grain refinement, weldability improvement, twin inhibition, and strength and hardness improvement [40]. During the friction stir welding, deformation-induced precipitation considered to be stimulated by the nucleation of dynamic recrystallized stimulate

precipitates [41]. Figure 7 shows the SEM results of the HAZ and BM in different cooling environment. In the BM, there were regions with element enrichment as shown in Fig. 7f. In the HAZ, the precipitations distributed diffuse and small when the cooling water temperature was 15 °C. With the increase of the cooling water temperature, the sizes of the particles increase as shown in Figure 7b–e. Figure 8 shows the EDS results of the WN in the cooling water temperature of 15 °C and 75 °C. In different cooling water temperatures, the WN was heated differently, and the precipitation of the microelements decreased with the increase of the cooling water temperature. Because of the heat increase, the solid solubility of Mn, Ce, Zn, and Al increased in the Mg matrix, so that the precipitation of the elements decreased. According to the Mg-Zn and Mg-Mn phase diagrams, Mg-Zn compounds experienced a phase transition with the increase of the Zn elements when the temperature was above 325 °C; the microstructure transformed from $\alpha(\text{Mg}) + \beta(\text{Mn})$ to $\alpha(\text{Mg}) + \alpha(\text{Mn})$ with the increase of the Mn elements when the temperature was above 300 °C [42]. α -Mn particles prefer to act as the heterogeneous nucleation sites of β rods and helps to promote the growth of β phase [43]. From Fig. 3, the WN of the different parameters are all above 325 °C,

**Fig. 12** SEM of the fracture section in different cooling water temperature. a 15 °C. b 30 °C. c 45 °C. d 60 °C. e 75 °C

which means that the materials would partly undergo the Mg-Zn and Mg-Mn phase transition in the WN.

4.3 Hardness

Microhardness was tested along the midline of the thickness direction, and the schematic diagram of the hardness points is shown in Fig. 9. The hardness curves present an inconspicuous “w”-type as shown in Fig. 9. The hardness of the BM is in the range of 47.0–48.3 HV_{0.1}. The trough hardness values appear at the transition area of AS and then rising rapidly to a stable level. At the RS side, the hardness of the TMAZ slowly decline, and another trough value appeared. The lowest value 44.4 HV_{0.1} located at the trough of the highest cooling water temperature of 75 °C. The highest hardness 56.2 HV_{0.1} was also the peak hardness of the cooling water temperature of 15 °C.

The grain size of the weld nugget affected the mechanical properties of the weld joint [44]. The transformation and flow of materials are different between the AS and the RS, and the heating temperature at the AS is higher than that of the RS [45]. A higher heating temperature resulted in larger grains and caused the decrease of the hardness, so that the lowest hardness was not located on the RS but on the AS. The WN experienced a stirring process and had a grain size that was finer than that of the base metal. The fine grains resulted in a high hardness value. The largest grains were found at the HAZ of the weld joint in the cooling water temperature of 75 °C. From Fig. 10, there is a decline of hardness value apart from the lowest hardness. As we know, HAZ is the weakest part of the joint with the lowest hardness; the rapid decline in hardness meant that the HAZ was small. Also, the hardness curves of the cooling water temperature of 75 °C showed that there was a slower decline at the trough position, which means that the region may be affected by the friction heat and had partial grain growth.

4.4 Tensile properties

Tensile samples are cut by a wire cutting machine according to the ASTM E8/E8M standard; the dimensions of the samples are shown in Fig. 11. The flash defects of the samples were ground off before the tensile tests. The average value of the two tensile samples was calculated to be the tensile strength value under different experimental conditions. The tensile strength and the fracture positions are shown in Table 2. The values of the strength present a downward trend as the cooling water temperature increased, but there was a break at the cooling water temperature of 15 °C, which presented the highest value of 170.5 MPa, which was ~ 71.04% of the BM. The lowest value is 161.0 MPa, ~ 67.06% of the BM when the cooling water temperature is 75 °C.

Because of the residual stress and dislocation content in the weld joint, the strength of the joints exhibits downtrend

compared with the raw metal after SFSW, which is generally proportional to the hardness in the metallic materials [46–48]. The fracture always located in regions with the lowest strength [49], as the same as the lowest hardness region, located at the HAZ of the AS, which was because the heat of the AS was higher than the RS, resulted in coarser grains. In addition, the grain boundaries between the transition region and the stir zone caused the fracture in the Mg alloy [50]. During the SFSW, the joints experienced annealing, and with the increase of the friction heat and annealing time, residual stress was partially eliminated. Great grain refinement, dissolution, and dispersion of eutectic networks and strong basal texture caused by FSW were also the effects of the tensile strength [51]. Generally, as the heat input decrease, the dynamic recrystallized grain size decreased, and the volume fraction of dispersed particles increased. The grain size grew larger, and the precipitations decreased with the decrease of cooling water temperature, which reduced the dispersion strengthening and fine-grain strengthening.

Figure 12 shows the SEM test result of the fracture section. All of the fractures present a mixture of cleavage fracture and ductile fracture. Fracture appearance of the tensile specimens has a large number of uniformly distributed dimples. As the cooling water temperature increases, the cleavage surfaces increase, and the dimples decrease. Besides, the dimples were finer and more homogeneous than the other samples when the cooling water temperature is 45 °C, which resulted in higher strength value. Cleavage fractures due to the stress concentration and ruptures at the grain boundary have many cleavage planes with low crystal surface index.

5 Conclusion

In this work, the ME20M magnesium alloy is friction stir-welded underwater with the cooling water temperature changed from 15 to 75 °C in the 15 °C spacing; the thermal histories were simulated and compared with the experimental results. The effects of SFSW on macrostructure, microstructure, hardness, and tensile properties of ME20M magnesium alloy were investigated.

The main conclusions were as follows:

1. ME20M magnesium alloys were joined by friction stir welding under different cooling water temperatures. The temperature fields were simulated by the ANSYS software in the same parameters. The numerical results showed that the simulated method can accurately predict the temperature history in the SFSW process.
2. Flash defects can be found when the cooling water temperature was much higher, and with the increase of the temperature, the quantity of the flashes increase. The grain

size and the precipitation size increase when the cooling water temperature increase.

3. The microhardness of the welded joint presents a slight “w”-type along the middle line of the thickness. The highest value of the hardness was 56.2 HV_{0.1} at the 15 °C cooling water temperature. The lowest hardness 44.4 HV_{0.1} occurs at the HAZ of the advancing side at the highest cooling water temperature.
4. With the increase of the cooling water temperature, the strength of the welded joint decrease. The tensile strength of the welded joint was 170.5 MPa at the cooling water temperature of 15 °C, which was ~ 71.04% of the base metal. When the cooling water temperature is 45 °C, the fracture surface had the finer and more homogeneous dimples than the other samples.

Funding information The study work of this paper is supported by the National Natural Science Foundation of China (Grant No. 51475232).

References

1. Michels W (2016) Magnesium alloys and their applications. *Mater Technol.* 13(3):121–122
2. Lentz M, Klaus M, Coelho RS, Schaefer N, Schmack F, Reimers W, Clausen B (2014) Analysis of the deformation behavior of magnesium-rare earth alloys Mg-2 pct Mn-1 pct rare earth and Mg-5 pct Y-4 pct rare earth by in situ energy-dispersive X-ray synchrotron diffraction and elasto-plastic self-consistent modeling. *Metall Mater Trans A* 45(12):5721–5735
3. Yu Y, He B, Jiang M, Lv Z, Man H (2016) Fatigue properties of welded butt joint and base metal of MB8 magnesium alloy [J]. *China Welding* 25(1):343–347
4. Dallmeier J, Huber O, Saage H, Eigenfeld K, Hilbig A (2014) Quasi-static and fatigue behavior of extruded ME21 and twin roll cast AZ31 magnesium sheet metals. *Mater Sci Eng A* 590(2):44–53
5. Gall S, Coelho RS, Müller S, Reimers W (2013) Mechanical properties and forming behavior of extruded AZ31 and ME21 magnesium alloy sheets. *Mater Sci Eng A* 579:180–187
6. Li X, Qi W (2013) Effect of initial texture on texture and microstructure evolution of ME20 Mg alloy subjected to hot rolling. *Mater Sci Eng* 560:321–331
7. Mishra RS, Ma ZY (2005) Friction stir welding and processing. *Mater Sci Eng R Rep* 50(1–2):1–78
8. Cao G, Zhang D, Chai F, Zhang W, Qiu C (2015) Superplastic behavior and microstructure evolution of a fine-grained Mg–Y–Nd alloy processed by submerged friction stir processing. *Mater Sci Eng A* 642:157–166
9. Rao HM, Rodriguez RI, Jordon JB, Barkey ME, Guo YB, Badarinarayan H, Yuan W (2014) Friction stir spot welding of rare-earth containing ZEK100 magnesium alloy sheets. *Mater Des* 56(4):750–754
10. Rodriguez RI, Jordon JB, Rao HM, Badarinarayan H, Yuan W, Kadiri HE, Allison PG (2014) Microstructure, texture, and mechanical properties of friction stir spot welded rare-earth containing ZEK100 magnesium alloy sheets. *Mater Sci Eng A* 618(10):637–644
11. Carlone P, Astarita A, Rubino F, Pasquino N (2015) Microstructural aspects in FSW and TIG welding of cast ZE41A magnesium alloy. *Metall Mater Trans B* 47(2):1340–1346
12. Carlone P, Palazzo GS (2015) Characterization of TIG and FSW weldings in cast ZE41A magnesium alloy. *J Mater Process Technol* 215:87–94
13. Pan F, Xu A, Deng D, Ye J, Jiang X, Tang A, Ran Y (2016) Effects of friction stir welding on microstructure and mechanical properties of magnesium alloy Mg-5Al-3Sn. *Mater Des* 110:266–274
14. Wang S, Zhang D (2011) Microstructure and mechanical properties of frictional stirring processing (FSP) MB8 magnesium alloy. *Special-cast and Non-ferrous Alloys.* 31(1):83–86
15. Xing L, Ke L, Sun D, Zhou X (2001) Friction-stir welding of MB8 magnesium alloy sheet. *Trans China Weld Inst.* 22(6):18–20
16. Xu W (2002) Friction stir welding of magnesium alloy MB8. *J Mater Eng.* 8:35–36
17. Darras B, Kishta E (2013) Submerged friction stir processing of AZ31 magnesium alloy. *Mater Des* 47(9):133–137
18. Luo X, Cao G, Zhang W, Qiu C, Zhang D (2017) Ductility improvement of an AZ61 magnesium alloy through two-pass submerged friction stir processing. *Materials* 10(3):253
19. Chai F, Zhang D, Li Y (2015) Microstructures and tensile properties of submerged friction stir processed AZ91 magnesium alloy. *J Aeronaut Mater* 3(3):203–209
20. Fu R, Sun Z, Sun R, Ying L, Liu H, Lei L (2011) Improvement of weld temperature distribution and mechanical properties of 7050 aluminum alloy butt joints by submerged friction stir welding. *Mater Des* 32(10):4825–4831
21. Guerdoux S, Fourment L (2009) A 3D numerical simulation of different phases of friction stir welding. *Modelling & Simulation in Materials Science & Engineering* 17(7):075001
22. Wen Q, Li W, Gao Y, Yang J, Wang F (2019) Numerical simulation and experimental investigation of band patterns in bobbin tool friction stir welding of aluminum alloy. *Int J Adv Manuf Technol.* 100: 2679–2687
23. Serindag HT, Kiral BG (2017) Friction stir welding of AZ31 magnesium alloys - a numerical and experimental study. *Lat Am J Solids Struct.* 14(1):113–130
24. Asadi P, Besharati Givi MK, Akbari M (2016) Simulation of dynamic recrystallization process during friction stir welding of AZ91 magnesium alloy. *Int J Adv Manuf Technol.* 83:301–311
25. Asadi P, Mahdavijad RA, Tutunchilar S (2011) Simulation and experimental investigation of FSP of AZ91 magnesium alloy. *Mater Sci Eng A.* 528:6469–6477
26. Ghetiya ND, Patel KM (2018) Numerical simulation on an effect of backing plates on joint temperature and weld quality in air and immersed FSW of AA2014-T6. *Int J Adv Manuf Technol.* 99(5–8):1937–1951
27. Chen G, Ma Q, Zhang S, Wu J, Zhang G, Shi Q (2018) Computational fluid dynamics simulation of friction stir welding: a comparative study on different frictional boundary conditions. *J Mater Sci Technol.* 34:128–134
28. Huang Y, Xie Y, Meng X, Lv Z, Cao J (2018) Numerical design of high depth-to-width ratio friction stir welding. *J Mater Process Tech.* 252:233–241
29. Hamilton C, Dymek S, Sommers A (2008) A thermal model of friction stir welding in aluminum alloys. *Int J Mach Tool Manuf.* 48(10):1120–1130
30. Zhang J, Shen Y, Li B, Xu H, Yao X, Kuang B, Gao J (2014) Numerical simulation and experimental investigation on friction stir welding of 6061-T6 aluminum alloy. *Mater Des.* 60:94–101
31. Schmidt H, Hattel J, Wert J (2004) An analytical model for the heat generation in friction stir welding. *Model Simul Mater Sci Eng* 12(1):143–157
32. Neto DM, Neto P (2013) Numerical modeling of friction stir welding process: a literature review [J]. *Int J Adv Manuf Technol* 65(1–4):115–126

33. Huang Y, Xie Y, Meng X, Li J, Zhou L (2019) Joint formation mechanism of high depth-to-width ratio friction stir welding. *J Mater Sci Technol* 35:1261–1269
34. Su H, Wu CS, Pittner A, Rethmeier M (2014) Thermal energy generation and distribution in friction stir welding of aluminum alloys. *Energy* 77:720–731
35. Riahi M, Nazari H (2011) Analysis of transient temperature and residual thermal stresses in friction stir welding of aluminum alloy 6061-T6 via numerical simulation. *Int J Adv Manuf Technol* 55: 143–152
36. Ghetiya ND, Patel KM, Anup BP (2015) Prediction of temperature at weldline in air and immersed friction stir welding and its experimental validation. *Int J Adv Manuf Technol* 79:1239–1246
37. Hajinezhad M, Azizi A (2016) Numerical analysis of effect of coolant on the transient temperature in underwater friction stir welding of Al6061-T6. *Int J Adv Manuf Technol* 83(5-8):1241–1252
38. Kim YG, Fujii H, Tsumura T, Komazaki T, Nakata K (2006) Three defect types in friction stir welding of aluminum die casting alloy. *Mater Sci Eng A*. 415(1-2):250–254
39. Zhang HJ, Liu HJ, Yu L (2011) Effect of water cooling on the performances of friction stir welding heat-affected zone. *J Mater Eng Perform*. 21(7):1182–1187
40. Pegguleryuz M, Kainer K, Kaya A A. (2013). Fundamentals of magnesium alloy metallurgy. index. 357-368.
41. Kabir ASH, Sanjari M, Su J, Jung I-H, Yue S (2014) Effect of strain-induced precipitation on dynamic recrystallization in Mg–Al–Sn alloys. *Mater Sci Eng A*. 616:252–259
42. Robson JD, Henry DT, Davis B (2011) Particle effects on recrystallization in magnesium–manganese alloys: particle pinning. *Mater Sci Eng A* 528(12):4239–4247
43. Shi G, Zhang D, Zhao X, Zhang K, Li X, Li Y, Ma M (2013) Precipitate evolution in Mg-6 wt% Zn-1 wt% Mn alloy. *Rare Metal Mater Eng* 42(12):2447–2452
44. Santos TG, Miranda RM, Vilaça P (2014) Friction stir welding assisted by electrical Joule effect. *J Mater Process Technol*. 214(10):2127–2133
45. Cao X, Jahazi M (2009) Effect of welding speed on the quality of friction stir welded butt joints of a magnesium alloy. *Mater Des*. 30(6):2033–2042
46. Hu Z, Dai M, Pang Q (2018) Influence of welding combined plastic forming on microstructure stability and mechanical properties of friction stir-welded Al-Cu alloy. *J Mater Eng Perf*. 27:4036–4042
47. Chen Y, He C, Yang K, Zhang H, Wang C, Wang Q, Liu Y (2019) Effects of microstructural inhomogeneities and micro-defects on tensile and very high cycle fatigue behaviors of the friction stir welded ZK60 magnesium alloy joint. *Int J Fatigue*. 122:218–227
48. Wang Y, Huang Y, Meng X, Wan L, Feng J (2017) Microstructural evolution and mechanical properties of Mg-Zn-Y-Zr alloy during friction stir processing. *J Alloys Compd* 696:875–883
49. Fu R, Sun Z, Sun R, Li Y, Liu H, Liu L (2011) Improvement of weld temperature distribution and mechanical properties of 7050 aluminum alloy butt joints by submerged friction stir welding. *Mater Des* 32:4825–4483
50. Vijayakumar S, Balaji J, Ramesh S, Prince J, L. L. (2019) Assessment of microstructure and mechanical properties of stir zone seam of friction stir welded magnesium AZ31B through Nano-SiC. *Mater*. 12:1044
51. Hartt WH, Reed-Hill RE (1968) Internal deformation and fracture of second-order {1011}–{1012} twins in magnesium. *Trans. Metall. Soc. AIME* 242:1127–1132

Publisher's note Springer Nature remains neutral with regard to jurisdictional claims in published maps and institutional affiliations.